Atomic-scale characterization of the interfacial phonon in graphene/SiC

Emi Minamitani,[1,*] Ryuichi Arafune,[2] Thomas Frederiksen,[3,4] Tetsuya Suzuki,[5] Syed Mohammad Fakruddin Shahed,[5] Tomohiro Kobayashi,[5] Norifumi Endo,[6] Hirokazu Fukidome,[6] Satoshi Watanabe,[1] and Tadahiro Komeda[5,†]

[1]*Department of Materials Engineering, The University of Tokyo, 7-3-1 Hongo, Bunkyo-ku, Tokyo 113-8656, Japan*

[2]*International Center for Materials Nanoarchitectonics (WPI-MANA), National Institute for Materials Science, 1-1 Namiki, Tsukuba, Ibaraki 304-0044, Japan*

[3]*Donostia International Physics Center, Paseo Manuel de Lardizabal, 4, E-20018 Donostia-San Sebastián, Spain*

[4]*IKERBASQUE, Basque Foundation for Science, E-48013 Bilbao, Spain*

[5]*Institute of Multidisciplinary Research for Advanced Materials, Tohoku University, 2-1-1 Katahira, Aobaku, Sendai, Miyagi 980-8577, Japan*

[6]*Research Institute of Electrical Communication, Tohoku University, 2-1-1 Katahira, Aoba-ku, Sendai 980-8577, Japan*

(Received 24 May 2017; published 11 October 2017)

Epitaxial graphene on SiC that provides wafer-scale and high-quality graphene sheets on an insulating substrate is a promising material to realize graphene-based nanodevices. The presence of the insulating substrate changes the physical properties of free-standing graphene through the interfacial phonon, e.g., limiting the mobility. Despite such known impacts on the material properties, a complete and microscopic picture is missing. Here, we report on atomically resolved inelastic electron tunneling spectroscopy (IETS) with a scanning tunneling microscope for epitaxial graphene grown on 4*H*-SiC(0001). Our data reveal a strong spatial dependence in the IETS spectrum, which cannot be explained by intrinsic graphene properties. We show that this variation in the IETS spectrum originates from a localized low-energy vibration of the interfacial Si atom with a dangling bond via *ab initio* electronic and phononic state calculations. This insight may help advancing graphene device performance through interfacial control.

DOI: 10.1103/PhysRevB.96.155431

I. INTRODUCTION

Graphene, a one-atom-thick honeycomb lattice of carbon with a novel electronic state equivalent to two-dimensional relativistic Dirac electrons, has attracted considerable attention since its discovery in 2004 [1–3]. Characteristics arising from the Dirac electron state, such as the anomalous quantum Hall effect (QHE) and ultrahigh mobility [2,4], make graphene a promising material for future nanoscale electronics. However, in order to incorporate graphene into field effect transistor architectures, large-scale synthesis on an insulating substrate is required. Thermal decomposition of SiC is one of the smart techniques for transfer-free wafer-scale epitaxial graphene growth to achieve this [5–9]. The measurements of Shubnikov–de Haas oscillations and QHE in the epitaxial graphene on SiC indicate high-quality and continuous monolayer growth, but at the expense of a strongly reduced mobility [10,11]. One of the dominant origins of this mobility reduction is electron-phonon scattering involving the substrate surface, as reported in previous studies [10,12,13]; however, the precise nature of the responsible interfacial phonon mode was not revealed.

A characteristic feature of the graphene/SiC interface is the presence of a C buffer layer beneath the graphene layer with a $6\sqrt{3} \times 6\sqrt{3}R30$ reconstructed structure, hereafter denoted by $6\sqrt{3}$ [8,14–16]. This superstructure is originated from several types of interfacial Si and buffer-layer C with different local atomic environments, i.e., with covalent Si-C bonds or dangling bonds. Previous *ab initio* calculations addressed how the interfacial electronic states are strongly affected by the local atomic environment and how this leads to spatial dependence [17–19], which suggests that the phonon properties should also show a spatial variation. Local measurements for revealing such correlations between the geometric structure and the phonon properties are key to understanding the interfacial phonon. For this purpose, we use scanning tunneling microscopy (STM) and demonstrate that information about phonons at the interface between graphene and SiC can be extracted from inelastic electron tunneling spectra (IETS). We detect phonon modes with energies of 9 and 24 meV, whose intensity change appears in a synchronized manner with the superstructure that appears in the topographic image. Based on density functional theory (DFT) calculations, we identify that the feature at 9 meV is derived from vibrations in graphene and the buffer layer, while the one at 24 meV is derived from the phonon mode associated with the interfacial Si atom possessing a dangling bond. Our combined experimental and theoretical results thus provide a detailed atomic-scale characterization of the interfacial geometric structure and the associated phonon properties.

II. STM AND STM-IETS EXPERIMENTS ON GRAPHENE/SiC

Our graphene/SiC sample was prepared by annealing a Si-terminated 4*H*-SiC(0001) substrate in an argon atmosphere of about 1 bar, which yields a top monolayer of graphene and a carbon buffer layer [1]. The SiC(0001) substrate was *n* type with a resistivity of 2 Ω cm. The angle-resolved photoemission spectrum taken on the sample prepared with the same condition exhibits a typical band dispersion of a monolayer graphene/buffer layer/SiC structure [20], which supports that the chemical composition and preparation procedures of our sample are appropriate. The sample was transferred into a

*eminamitani@cello.t.u-tokyo.ac.jp
†komeda@tagen.tohoku-u.ac.jp

UHV chamber, where it was heated to 573 K to remove residual contaminations before being moved to the STM head. In the STM/scanning tunneling spectroscopy (STS) experiments, the sample temperature was ∼4.7 K. STS spectra were obtained using a lock-in amplifier with a modulation voltage of 2 mV superimposed onto the tunneling bias voltage.

A typical topographic image of epitaxial graphene grown on a Si-terminated 4H-SiC(0001) surface is shown in Fig. 1(a). The larger size of this topographic image is shown in the Supplemental Material (Fig. S1) [21]. In the image, in addition to the protrusions of atoms, a long-range superstructure with the $6\sqrt{3} \times 6\sqrt{3}R30$ ($6\sqrt{3}$) reconstruction is visible, which is consistent with the results of previous work [22–24]. The two areas specified by arrows are labeled as bright (B) and dark (D), respectively. The dI/dV spectra obtained by placing the STM tip on the B and D areas are shown in Fig. 1(b). Both spectra reveal a dip around −130 meV and a gap near the Fermi level. The former feature resembles the Dirac point, but we found that the more obvious dip structure appears around −400 meV in the wide-range STS spectrum (Fig. S2). Comparing the STS spectrum with the previous angle-resolved photoemission spectroscopy (ARPES) results that show a Dirac point around −400 meV, we assign the dip around −400 meV to the Dirac point and speculate that the dip around −130 meV originates from a different origin, such as the electronic state of the substrate or interface. Whereas this dip structure around −130 meV has little spatial dependence, the gap near the Fermi level shows a marked dependence on the tip position; the gap measured at B is wider than that at D.

Such spatial dependence of the gap structure in the dI/dV spectrum is hardly explained by the intrinsic electronic structure of graphene. One possible origin is phonon excitations at the interface via an inelastic tunneling process [25–31]. As schematically shown in Fig. 1(c), the excitation of the phonon caused by the tunneling electron appears as a staircase in dI/dV and/or a peak-dip pair in d^2I/dV^2 that is positioned at the energy of the phonon. These characteristic spectral features indeed appear in dI/dV and d^2I/dV^2 obtained at B and D [Figs. 1(d) and 1(e)]. The results obtained at B show a staircase increase in dI/dV, which corresponds to the peak at +24 meV and the dip at −24 meV in the d^2I/dV^2 spectrum [see the arrows in Fig. 1(d)]. On the other hand, dI/dV obtained at D shows a much narrower gap and the peak and dip can be seen at ±9 meV, as shown by the arrows in the figure.

The spatial distributions of dI/dV and d^2I/dV^2 are shown more clearly in the mapping image for the spectra obtained along the line connecting the centers of neighboring bright spots and dark areas. In Fig. 1(f), we illustrate an example of the dI/dV (d^2I/dV^2) mapping image in the left-hand (right-hand) side panel together with a topographic image at the center that indicates the measured positions. As far as we can judge from the topographic image, the surface area where we measured dI/dV and d^2I/dV^2 is free from interfacial defects, and the effects of the defects can be ruled out from the origin of the spatial distribution.

As can be seen in the dI/dV mapping, the measured conductance around the Fermi level is low at all measured positions. A rapid increase of the conductance appears as positive/negative bias voltage increases at both ends of the vertical direction (corresponding to the D position). However,

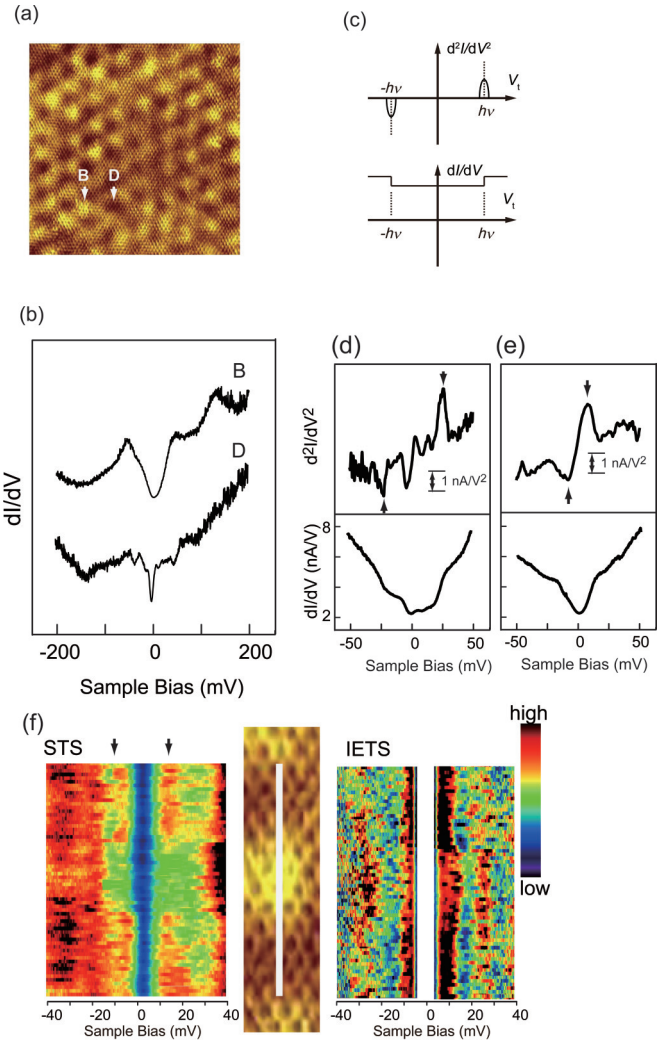

FIG. 1. (a) STM topographic image of epitaxial graphene grown on a SiC(0001) surface. Area 14 × 14 nm^2, and set point of I = 0.8 nA and V = −200 mV. The brighter color represents the charge accumulation. (b) STS spectra obtained at the bright (B) and dark (D) areas of the topographic image. (c) Schematics of dI/dV (STS) and d^2I/dV^2 (IETS) spectra for an excitation of a phonon with an excitation energy of $h\nu$. (d), (e) dI/dV and d^2I/dV^2 spectra obtained at B and D areas. Black arrows in (d) and (e) indicate the energy at which the prominent inelastic phonon excitation occurs. (f) Spatial distribution of dI/dV (left panel) and d^2I/dV^2 (right panel). The series of dI/dV and d^2I/dV^2 is taken along the white line that connects the neighboring bright spots in the STM topographic image shown in the center panel. The horizontal axis corresponds to the sample bias and the vertical axis corresponds to the measured position (corresponding directly to the right panel) and the intensity of the d^2I/dV^2 spectrum is expressed according to a color table. For d^2I/dV^2, the contrast is reversed in the positive and negative energy regions for a clear view.

this cannot be seen in the middle of the vertical direction (B position) where the conductance increases slowly.

In the d^2I/dV^2 mapping obtained simultaneously, we see the highlighted d^2I/dV^2 feature (corresponding to the dark brown color) at ±9 meV when measured near the D area. When moved to the B area, this feature is weakened in intensity

and features near ±24 meV appear. This coincides with the characteristic features described in Figs. 1(d) and 1(e).

The gap structure around the Fermi level induced by phonon excitations has been reported in graphene on SiO_2 [32,33] and SiC [34]. In Refs. [32,33], the gap formation is explained by the excitation of an intrinsic graphene phonon mode with a wave number close to the K/K' point in the Brillouin zone. The gap size induced by this phonon mode is 120 meV and there is no spatial dependence, which is much different from the behavior of the feature observed in our experiment. In Ref. [34], spatial dependence in the phonon excitation spectrum is also reported. However, there is no correlation with $6\sqrt{3}$ periodicity, and the modulation of the spectrum is attributed to the interfacial defect. These results imply that a different mechanism and the phonon mode contribute to the gap structure formation in our system.

III. THEORETICAL ANALYSIS BASED ON *AB INITIO* CALCULATIONS

In order to elucidate these points, we carried out a theoretical analysis based on *ab initio* calculations. First, we assigned the correspondence between the interfacial atomic structure and brightness in the STM topographic image. STM simulation is carried out using the Vienna *ab initio* simulation package (VASP) [35,36] with a projected augmented wave (PAW) pseudopotential [37]. In the VASP calculations, we set the cutoff energy to 400 eV. Because of the large dimensions of the supercell, the Brillouin zone was sampled with a single k point only at the $\bar{\Gamma}$ point. We use the local-density approximation exchange-correlation functional determined by Ceperly and Alder [38] and parametrized by Perdew and Zunger [39]. The STM simulation is carried out based on the Tersoff-Haman approximation [40].

Figure 2(a) is the STM simulation result for a $6\sqrt{3}$ structure with bias voltage of −100 meV. Figure 2(b) shows the partial charge density in the energy range between −100 and 0 meV, which is used to illustrate the STM simulation result. From the cross-sectional image of the partial charge density [Figs. 2(c) and 2(d)], we found that the point with the highest charge density, i.e., the brightest point in the STM simulation result, corresponds to the dangling bond of the Si atom at the interface. In contrast, the interfacial Si atoms placed beneath the buffer layer C atom exhibit less partial charge density and correspond to the dark area in the topographic image. This is because the dangling bond state placed around the Fermi level is saturated by the formation of a covalent bond with the C atom in the buffer layer. From these results, we conclude that the dangling bond of the interfacial Si determines the contrast of the STM topographic image.

Considering the correlation between the STM topographic image and the spatial dependency in the IETS signal, we surmised that the Si dangling bond gives rise to the difference in the IETS signal. In order to confirm the relation between the Si dangling bond and the IETS signal, we carried out *ab initio* calculations of the overall phonon properties, and the dI/dV spectra including inelastic scattering. In these calculations, we used the smaller structural model shown in Fig. 3(a) in order to reduce the computational cost. This $\sqrt{3} \times \sqrt{3}R30$ model, hereafter denoted by $\sqrt{3}$, also contains the typical atomic local

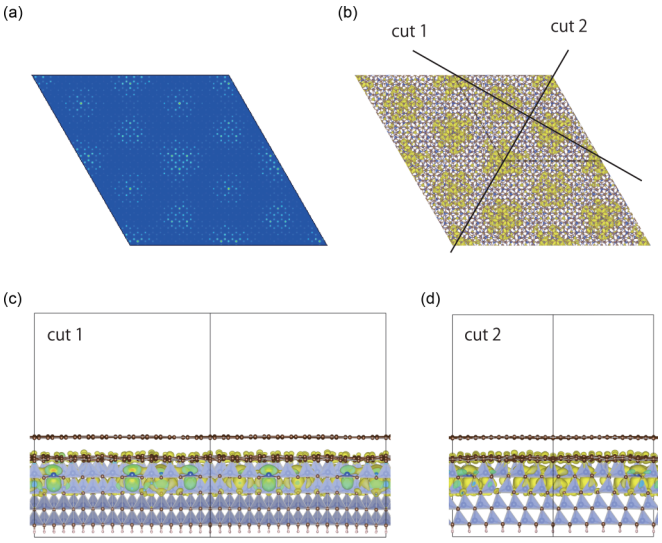

FIG. 2. (a) STM simulation results at −100 mV sample bias voltage. (b) Partial charge distribution used for plotting (a). The black lines indicate the planes where the cross-sectional views shown in (c) and (d) are taken. (c), (d) Cross-sectional images of the partial charge distribution taken on the cut 1 and cut 2 plane in (b), respectively. The blue-gray surfaces are the tetrahedron of C centered by a Si atom. The charge distribution becomes dense at the Si atom with a dangling bond that is not surrounded by the tetrahedral plane.

environments from the $6\sqrt{3}$ structure: the relative position between C atoms in the topmost graphene layer and the buffer layer, and the interfacial Si atom. The C atoms in the graphene can be classified into four types, indicated by the different colors in the right panel of Fig. 3(a). C1 type atoms (light green) are positioned on top of both the buffer C atom and interfacial Si atom. C2 type atoms (light blue) are positioned on top of the buffer C atom; however, there is no interfacial Si atom beneath. Below the C3 type atoms (orange), there is no buffer C atom or interfacial Si atom. C4 type atoms (pink) are positioned on top of the interfacial Si atom with the dangling bond. The C atoms in the buffer layer are classified according to the presence or absence of C-Si bonding, and the Si atoms are distinguished according to the presence or absence of the dangling bond. It is well accepted that this model well reproduces the ARPES experimental results [19] and the Raman spectra from the buffer layer [41].

We first analyze the phonon band dispersion and density of states (DOS) projected on the respective types of atoms mentioned above. These phonon properties in the $\sqrt{3}$ model are calculated by using density functional perturbation theory (DFPT) [42] implemented in the QUANTUM ESPRESSO (QE) package [43]. In these calculations, we use the ultrasoft pseudopotential generated with the Rappe, Rabe, Kaxiras, and Joannopoulos (RRKJ3) [44] scheme for Si, C, and H atoms. The local-density approximation exchange-correlation functional was used. The expansion of the plane-wave basis set was restricted by a kinetic energy cutoff of 48 Ry. For the phonon calculations, we set the charge density cutoff to 400 Ry. A 6 × 6 × 1 Monkhorst-Pack grid [45] without an offset was used for the ionic relaxation and self-consistent electronic structure calculations. The atoms in the slab were fully relaxed

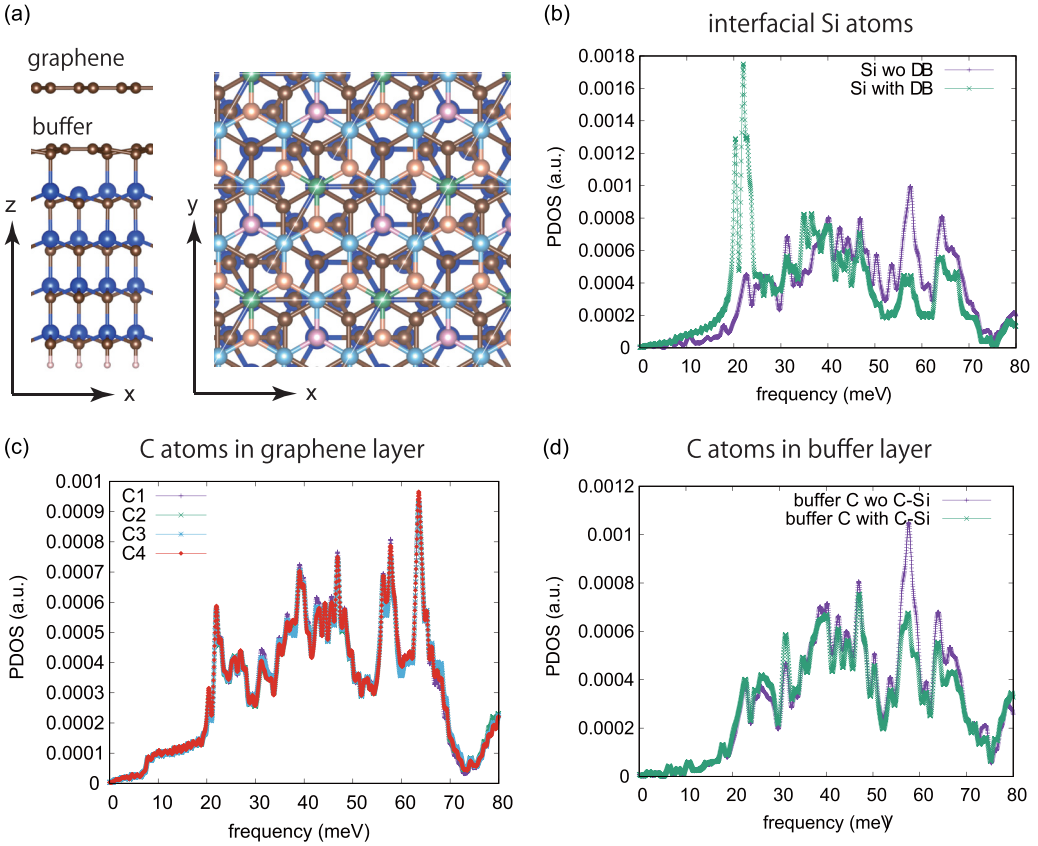

FIG. 3. (a) Geometric structure of the $\sqrt{3}$ model of epitaxial graphene on 4H-SiC (0001). Left: Side view of the structure; brown, C; blue, Si; light pink, H atoms. Right: Top view of the structure. The four different colors of the C atoms in the topmost graphene layer correspond to the different chemical environments; light green, C1 type atoms positioned on the top of the buffer C and interfacial Si atom; light blue, C2 type atoms also positioned on top of the buffer C atom, but with no interfacial Si atom beneath; orange, C3 type atoms where there is no buffer C atom or interfacial Si atom beneath; pink, C4 type atoms positioned on the top of the interfacial Si atom with dangling bond. (b)–(d) Phonon DOS of the z-polarized mode projected on the interfacial Si atoms, the C atoms in the graphene layer, and the C atoms in the buffer layer, respectively.

without any constraint until the forces on individual atoms were less than 1.0×10^{-4} a.u. before the phonon calculations. The phonon dispersion was calculated by DFPT on the uniform $3 \times 3 \times 1$ grid in the surface Brillouin zone.

The results of the projected phonon band dispersion are shown in the Sec. II of the Supplemental Material [21]. Comparing the phonon dispersion projected along the x, y, and z directions, it is apparent that a contribution from the z-polarized mode is dominant in the low-energy region below 50 meV. Therefore, we focus on the z-polarized mode in the following discussion of the projected phonon DOS. The projected phonon DOS obtained at the interfacial Si atoms indeed shows a clear spatial dependence [Fig. 3(b)]. The pronounced peak structure around 24 meV only appears for the Si atoms with the dangling bond, and disappears for the Si atoms without the dangling bond. This peak originates from the strongly localized vibration in the z direction at the Si atom with the dangling bond, which appears as the flat phonon dispersion in Supplemental Fig. S4(c) [21]. The phonon DOS projected on the C atoms in the top graphene layer shows a negligible difference among C1–C4 type atoms [Fig. 3(c)]. The phonon band dispersion in the top graphene layer is almost the same as that in the free-standing graphene, except for the shift in phonon energy due to the extension of the lattice constant in this model (see Sec. IV in the Supplemental Material [21]). Therefore, the spatial dependence observed in STM-IETS does not originate from the intrinsic phonon mode in graphene. For the phonon mode of the buffer layer C atom, the phonon DOS depends on whether there is a bond between the C atom and the interfacial Si atom [Fig. 3(d)]. However, this difference is mainly distributed in the higher-frequency range (>80 meV), and does not provide an explanation for the spatial distribution of STM-IETS in the low-energy region below 50 meV.

From the above discussion on the phonon DOS, the spatial dependency of the low-energy phonon excitations is attributed to the variation of interfacial Si atoms with or without dangling bonds. To connect these phonon properties to the experimental results, we also simulated the dI/dV spectrum. We selected two representative model structures for the dark (D) and bright (B) regions, as shown in Fig. 4(a). In the D(B) model, the STM tip apex is represented by a chain of gold atoms placed above the graphene C atom positioned on top of the Si atom without (with) a dangling bond, respectively [46]. The electronic structure, geometries, and dynamical matrix in these two model structures are calculated with the SIESTA code [47]. Atomic coordinates in the "dynamical" region in Fig. 4(a) are relaxed until the force acting on respective atoms becomes smaller than 0.02 eV/A. The dynamical matrix is evaluated

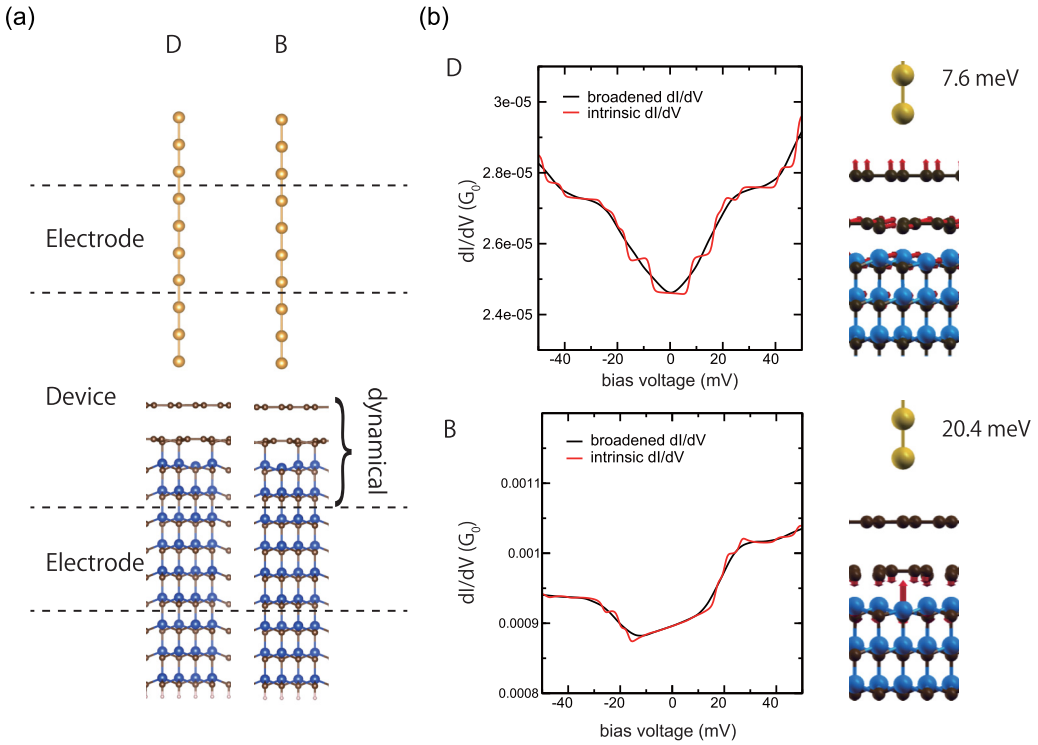

FIG. 4. (a) Two structure models (D and B) used in the dI/dV calculations. (b) dI/dV simulations in the D and B models. Black lines are dI/dV taking into account the extra broadening from the lock-in measurement technique ($V_{\mathrm{rms}} = 5$ meV). Red lines are the intrinsic dI/dV results (linewidth only due to a finite temperature of $T = 4.2$ K). The structural side views show the displacements of the atoms in the active phonon modes that contribute to the narrow (7.6 meV) and wide (20.4 meV) gaps, respectively.

from the finite difference for the atoms in this region. The basis set consisting of double-zeta plus polarization orbitals is used for all atoms in the model. The exchange correlation is described by the generalized gradient approximation (GGA) [48]. We set the cutoff at 400 Ry for the real-space grid integration and the $9 \times 9 \times 1$ Monkhorst-Pack sampling of the Brillouin zone. In order to reproduce the n-doped state in SiC, we adopt the virtual crystal approximation (VCA) [49] for the C atoms in SiC; the pseudopotential for these atoms is replaced by a mixture of 99.5% C and 0.5% N pseudopotentials. The transport properties are simulated with the TRANSIESTA two-terminal setup [47,50]. The scattering (device) region and the unit cell for two semi-infinite electrodes are also shown in Fig. 4(a). The transport calculation is restricted to the M point of the two-dimensional Brillouin zone where the conduction band minimum in the n-doped SiC electrode touches the Fermi level (see Fig. S12 [21]). The dI/dV spectra, including electron-phonon scattering, was computed using INELASTICA [51].

The obtained results are in good agreement with the experimental findings [Fig. 4(b)]. First, the intensity of the dI/dV spectrum is much larger in the B model than in the D model calculated with the same tip-sample distance, which reproduces the bright/dark contrast in the STM topographic image. Second, the shape of the dI/dV spectra for both D and B (in particular, those taking into account the broadening from the experimental lock-in measurement technique) matches those measured in the dark and bright areas; the gap in the dI/dV spectrum is much wider (~40 meV) in the B model than in the D model (~20 meV). The intrinsic dI/dV results (i.e., temperature broadening only) show that the phonon mode of 20.4 meV is the origin of the wide gap structure in the B model. As shown in Fig. 4(b), this phonon mode corresponds to the vertical motion of the interfacial Si atom with the dangling bond, which is the same phonon mode that appears as a sharp peak structure in the phonon DOS shown in Fig. 3(c). In addition to this mode, the low-frequency phonon mode of 7.6 meV, which mainly consists of the out-of-plane vibration of the outermost graphene layer and in-plane vibration of the buffer layer C atoms, is excited in the D model.

IV. SUMMARY

We observed the interfacial phonon mode through atomically resolved STM-IETS on epitaxial graphene grown on a SiC (0001) surface. The dI/dV spectra exhibit a strong spatial dependence that correlates with the STM topographic image; the gap in the dI/dV spectrum taken at the dark (bright) area in the STM image is 18 meV (48 meV). The theoretical analysis using *ab initio* calculations reveals that the spatial dependence in the dI/dV spectrum originates from the presence/absence of the dangling bond at the interfacial Si atom. The gap of 48 meV in the dI/dV spectrum taken at the bright area is attributed to the localized z-polarized vibration of the interfacial Si atom with a dangling bond, which is not present in the dark region due to the saturation of the Si dangling bond by the buffer layer. The interfacial phonon with 24 meV reported here is different from the phonons

studied in previous investigations, e.g., the optical phonon mode of the SiC surface [52,53], the interlayer longitudinal optical mode [53], vibration of interfacial defects [34], and the acoustic mode of the buffer layer [13]. In addition, this interfacial phonon mode is optical, as can be seen from its flatband dispersion, which would induce the remote-interfacial phonon (RIP) scattering [52]. Considering its low energy, this phonon mode would be active at room temperature and become a source of RIP scattering which degrades the carrier mobility. Our results thus provide a deeper understanding of the interfacial phonon in graphene on the SiC substrate, which could help advance the performance of graphene nanodevices.

ACKNOWLEDGMENTS

The following financial supports are acknowledged: Grant-in-Aid for Scientific Research on Innovative Areas (MEXT KAKENHI Grants No. JP25110005 (Tadahiro K.), No. JP26102017 (E.M.), and No. JP2511008 (R.A.)), JSPS KAKENHI Grants No. JP17K19047 (Tadahiro K.), No. JP16H03863 (Tadahiro K.), No. JP15H03561 (E.M. and S.W.), and No. JP17H05215 (E.M. and S.W.), World Premier International Research Center Initiative (WPI) (R.A.), and the Basque Government (Dep. de Educación) through Grant No. PI-2016-1-0027 (T.F.).

[1] A. K. Geim and K. S. Novoselov, Nat. Mater. **6**, 183 (2007).
[2] K. S. Novoselov, A. K. Geim, S. V. Morozov, D. Jiang, M. I. Katsnelson, I. V. Grigorieva, S. V. Dubonos, and A. A. Firsov, Nature (London) **438**, 197 (2005).
[3] K. S. Novoselov, A. K. Geim, S. V. Morozov, D. Jiang, Y. Zhang, S. V. Dubonos, I. V. Grigorieva, and A. A. Firsov, Science **306**, 666 (2004).
[4] Y. Zhang, Y.-W. Tan, H. L. Stormer, and P. Kim, Nature (London) **438**, 201 (2005).
[5] C. Berger, Z. Song, X. Li, X. Wu, N. Brown, C. Naud, D. Mayou, T. Li, J. Hass, A. N. Marchenkov, E. H. Conrad, P. N. First, and W. A. de Heer, Science **312**, 1191 (2006).
[6] A. Bostwick, T. Ohta, T. Seyller, K. Horn, and E. Rotenberg, Nat. Phys. **3**, 36 (2007).
[7] K. V. Emtsev, A. Bostwick, K. Horn, J. Jobst, G. L. Kellogg, L. Ley, J. L. McChesney, T. Ohta, S. A. Reshanov, J. Röhrl, E. Rotenberg, A. K. Schmid, D. Waldmann, H. B. Weber, and T. Seyller, Nat. Mater. **8**, 203 (2009).
[8] I. Forbeaux, J. M. Themlin, and J. M. Debever, Phys. Rev. B **58**, 16396 (1998).
[9] T. Ohta, A. Bostwick, T. Seyller, K. Horn, and E. Rotenberg, Science **313**, 951 (2006).
[10] J. Jobst, D. Waldmann, F. Speck, R. Hirner, D. K. Maude, T. Seyller, and H. B. Weber, Phys. Rev. B **81**, 195434 (2010).
[11] A. Tzalenchuk, S. Lara-Avila, A. Kalaboukhov, S. Paolillo, M. Syväjärvi, R. Yakimova, O. Kazakova, T. J. Janssen, V. Fal'ko, and S. Kubatkin, Nat. Nanotechnol. **5**, 186 (2010).
[12] J. L. Tedesco, B. L. VanMil, R. L. Myers-Ward, J. M. McCrate, S. A. Kitt, P. M. Campbell, G. G. Jernigan, J. C. Culbertson, C. R. Eddy, Jr., and D. K. Gaskill, Appl. Phys. Lett. **95**, 122102 (2009).
[13] N. Ray, S. Shallcross, S. Hensel, and O. Pankratov, Phys. Rev. B **86**, 125426 (2012).
[14] P. Mallet, F. Varchon, C. Naud, L. Magaud, C. Berger, and J. Y. Veuillen, Phys. Rev. B **76**, 041403 (2007).
[15] C. Riedl, U. Starke, J. Bernhardt, M. Franke, and K. Heinz, Phys. Rev. B **76**, 245406 (2007).
[16] F. Varchon, R. Feng, J. Hass, X. Li, B. N. Nguyen, C. Naud, P. Mallet, J.-Y. Veuillen, C. Berger, E. H. Conrad, and L. Magaud, Phys. Rev. Lett. **99**, 126805 (2007).
[17] M. Kajihara, T. Suzuki, S. M. F. Shahed, T. Komeda, E. Minamitani, and S. Watanabe, Surf. Sci. **647**, 39 (2016).
[18] S. Kim, J. Ihm, H. J. Choi, and Y.-W. Son, Phys. Rev. Lett. **100**, 176802 (2008).
[19] A. Mattausch and O. Pankratov, Phys. Rev. Lett. **99**, 076802 (2007).
[20] T. Someya, H. Fukidome, Y. Ishida, R. Yoshida, T. Iimori, R. Yukawa, K. Akikubo, Sh. Yamamoto, S. Yamamoto, T. Yamamoto, T. Kanai, K. Funakubo, M. Suemitsu, J. Itatani, F. Komori, S. Shin, and I. Matsuda, Appl. Phys. Lett. **104**, 161103 (2014).
[21] See Supplemental Material at http://link.aps.org/supplemental/10.1103/PhysRevB.96.155431 for supplemental STM/STS data and DFT calculation results.
[22] G. M. Rutter, J. N. Crain, N. P. Guisinger, T. Li, P. N. First, and J. A. Stroscio, Science **317**, 219 (2007).
[23] G. M. Rutter, N. P. Guisinger, J. N. Crain, E. A. A. Jarvis, M. D. Stiles, T. Li, P. N. First, and J. A. Stroscio, Phys. Rev. B **76**, 235416 (2007).
[24] T. Seyller, K. V. Emtsev, K. Gao, F. Speck, L. Ley, A. Tadich, L. Broekman, J. D. Eiley, R. C. G. Leckey, O. Rader, A. Varykhalov, and A. M. Shikin, Surf. Sci. **600**, 3906 (2006).
[25] H. Ueba, S. G. Tikhodeev, and B. N. J. Persson, in *Current-Driven Phenomena in Nanoelectronics*, edited by T. Seideman (Pan Stanford Publishing, Singapore, 2010), Chap. 2.
[26] W. Ho, J. Chem. Phys. **117**, 11033 (2002).
[27] J. Jandke, P. Hlobil, M. Schackert, W. Wulfhekel, and J. Schmalian, Phys. Rev. B **93**, 060505 (2016).
[28] T. Komeda, Prog. Surf. Sci. **78**, 41 (2005).
[29] E. Minamitani, R. Arafune, N. Tsukahara, Y. Ohda, S. Watanabe, M. Kawai, H. Ueba, and N. Takagi, Phys. Rev. B **93**, 085411 (2016).
[30] J. I. Pascual, Eur. Phys. J. D **35**, 327 (2005).
[31] M. Schackert, T. Märkl, J. Jandke, M. Hölzer, S. Ostanin, E. K. U. Gross, A. Ernst, and W. Wulfhekel, Phys. Rev. Lett. **114**, 047002 (2015).
[32] Y. Zhang, V. W. Brar, F. Wang, C. Girit, Y. Yayon, M. Panlasigui, A. Zettl, and M. F. Crommie, Nat. Phys. **4**, 627 (2008).
[33] T. O. Wehling, I. Grigorenko, A. I. Lichtenstein, and A. V. Balatsky, Phys. Rev. Lett. **101**, 216803 (2008).
[34] J. Červenka, K. van de Ruit, and C. F. J. Flipse, Phys. Rev. B **81**, 205403 (2010).
[35] G. Kresse and J. Furthmüller, Phys. Rev. B **54**, 11169 (1996).
[36] G. Kresse and J. Furthmüller, Comput. Mater. Sci. **6**, 15 (1996).
[37] P. E. Blöchl, Phys. Rev. B **50**, 17953 (1994).
[38] D. M. Ceperley and B. J. Alder, Phys. Rev. Lett. **45**, 566 (1980).
[39] J. P. Perdew and A. Zunger, Phys. Rev. B **23**, 5048 (1981).

[40] J. Tersoff and D. R. Hamann, Phys. Rev. B **31**, 805 (1985).
[41] F. Fromm, J. M. H. Oliveira, A. Molina-Sánchez, M. Hundhausen, J. M. J. Lopes, H. Riechert, L. Wirtz, and T. Seyller, New J. Phys. **15**, 043031 (2013).
[42] S. Baroni, S. de Gironcoli, A. Dal Corso, and P. Giannozzi, Rev. Mod. Phys. **73**, 515 (2001).
[43] P. Giannozzi, S. Baroni, N. Bonini, M. Calandra, R. Car, C. Cavazzoni, D. Ceresoli, G. L. Chiarotti, M. Cococcioni, I. Dabo, A. D. Corso, S. de Gironcoli, S. Fabris, G. Fratesi, R. Gebauer, U. Gerstmann, C. Gougoussis, A. Kokalj, M. Lazzeri, L. Martin-Samos, N. Marzari, F. Mauri, R. Mazzarello, S. Paolini, A. Pasquarello, L. Paulatto, C. Sbraccia, S. Scandolo, G. Sclauzero, A. P. Seitsonen, A. Smogunov, P. Umari, and R. M. Wentzcovitch, J. Phys.: Condens. Matter. **21**, 395502 (2009).
[44] A. M. Rappe, K. M. Rabe, E. Kaxiras, and J. D. Joannopoulos, Phys. Rev. B **41**, 1227 (1990).
[45] H. J. Monkhorst and J. D. Pack, Phys. Rev. B **13**, 5188 (1976).
[46] While this tip model implies that the 5*d* states of Au move up around the Fermi level, we have checked that their contribution to the present dI/dV simulations is negligible.
[47] J. M. Soler, E. Artacho, J. D Gale, A. García, J. Junquera, P. Ordejón, and D. Sánchez-Portal, J. Phys.: Condens. Matter **14**, 2745 (2002); M. Brandbyge, J.-L. Mozos, P. Ordejón, J. Taylor, and K. Stokbro, Phys. Rev. B **65**, 165401 (2002).
[48] J. P. Perdew, K. Burke, and M. Ernzerhof, Phys. Rev. Lett. **77**, 3865 (1996).
[49] P. Roberta, Í. Jorge, G. Alberto, and C. Enric, J. Phys.: Condens. Matter **22**, 415401 (2010).
[50] N. Papior, N. Lorente, T. Frederiksen, A. García, and M. Brandbyge, Comput. Phys. Commun. **212**, 8 (2017).
[51] T. Frederiksen, M. Paulsson, M. Brandbyge, and A.-P. Jauho, Phys. Rev. B **75**, 205413 (2007); INELASTICA is freely available at http://sourceforge.net/projects/inelastica.
[52] S. Fratini and F. Guinea, Phys. Rev. B **77**, 195415 (2008).
[53] R. J. Koch, S. Fryska, M. Ostler, M. Endlich, F. Speck, T. Hänsel, J. A. Schaefer, and T. Seyller, Phys. Rev. Lett. **116**, 106802 (2016).